Computational Mechanics (2023) 71:657–675
https://doi.org/10.1007/s00466-022-02256-w

ORIGINAL PAPER

T-splines computational membrane–cable structural mechanics with continuity and smoothness: I. Method and implementation

Takuya Terahara[1] · Kenji Takizawa[1] · Tayfun E. Tezduyar[2,3]

Received: 21 October 2022 / Accepted: 30 November 2022 / Published online: 8 January 2023

Abstract
We present a T-splines computational method and its implementation where structures with different parametric dimensions are connected with continuity and smoothness. We derive the basis functions in the context of connecting structures with 2D and 1D parametric dimensions. Derivation of the basis functions with a desired smoothness involves proper selection of a scale factor for the knot vector of the 1D structure and results in new control-point locations. While the method description focuses on C^0 and C^1 continuity, paths to higher-order continuity are marked where needed. In presenting the method and its implementation, we refer to the 2D structure as "membrane" and the 1D structure as "cable." It goes without saying that the method and its implementation are applicable also to other 2D–1D cases, such as shell–cable and shell–beam structures. We present test computations not only for membrane–cable structures but also for shell–cable structures. The computations demonstrate how the method performs.

Keywords Isogeometric analysis · T-splines · Membrane–cable structure · Shell–cable structure · Shell–beam structure · Continuity · Smoothness

1 Introduction

The isogeometric analysis (IGA), with the superior accuracy it offers, brought fluid and solid mechanics computations to a new level [1–4]. Being able to use the IGA basis functions also in time in the context of space–time (ST) computational analysis expended the scope of the IGA and led to the introduction of the ST-IGA [5–7]. The terminology "ST-IGA" implies, depending on the context, discretization with IGA basis functions in space or time or both. In the 2D test cases reported in [5], the computation of flow past an airfoil was with IGA basis functions in space, and the advection computations with IGA basis functions in both space and time. The advection computations, accompanied by a stability and accuracy analysis for the pure equation, showed the advantages of using higher-order basis functions, not only in space, but also in time. Related to that, keeping in mind that the increased accuracy the ST-IGA with IGA basis functions in space brings is attained with fewer control points, the effective element sizes will be larger. With that, larger time steps can be taken while still keeping the Courant number at or below the levels we target for good accuracy.

Using IGA basis functions in time is uniquely offered by the ST framework, and partly because of that the effort was focused on that track in the early years of the ST-IGA computations [5,6,8]. Taking advantage of that opportunity brings higher accuracy in representing the motion of a solid surface, a mesh motion consistent with that surface motion, and better efficiency in representing the mesh motion and in remeshing. The ST/NURBS Mesh Update Method (STNMUM) [6,9] was built around these positive attributes of the ST-IGA. Using IGA basis functions in time with C^2 continuity was instrumental in obtaining good-quality solutions in flapping-wing aerodynamics computations [6,10–15]. The method "ST-C" another example of the good continuity property of the ST-IGA with IGA basis functions in time. The

✉ Kenji Takizawa
Kenji.Takizawa@tafsm.org

Tayfun E. Tezduyar
tezduyar@tafsm.org

[1] Department of Modern Mechanical Engineering, Waseda University, 3-4-1 Ookubo, Shinjuku-ku, Tokyo 169-8555, Japan

[2] Mechanical Engineering, Rice University – MS 321, 6100 Main Street, Houston, TX 77005, USA

[3] Faculty of Science and Engineering, Waseda University, 3-4-1 Ookubo, Shinjuku-ku, Tokyo 169-8555, Japan

letter "C" in "ST-C" means "continuous." This is a method for extracting time-continuous data from the computed data, and it can work as a data compression method in dealing with large data volumes [16–29]. The classes of problems computed by using the ST-IGA with IGA basis functions in time include wind turbines [9,24,25,30–33], turbomachinery [7,20,21,24,25,34,35], flapping-wing aerodynamics [6,10–15], spacecraft cover separation aerodynamics [36], and higher-order temporal IGA discretization [37].

The classes of problems computed by using the ST-IGA with IGA basis functions in space include wind turbines [24–28,32,33], turbomachinery [7,20,21,24,25,34,35], ground vehicles and tires [29,33,38–43], fluid films [40,43,44], parachutes [22,23,45,46], cardiovascular medicine [47–57], Taylor–Couette flow [58], U-ducts [58], higher-order temporal IGA discretization [37], boundary-layer mesh resolution studies [59], and long-wake flows [60].

Moving to solid and structural mechanics computations with IGA basis functions in space, it was pointed out as early as in 2007 (see [61]) that the image-based geometries used in patient-specific arterial FSI computations are not for the zero-stress state (ZSS) of the artery and that a ZSS estimation method is needed. The ZSS estimation methods introduced in and after 2016 [51,62–65] stand on the IGA basis functions in space, and so does the related hyperelastic shell analysis [66,67]. The IGA basis functions in space have been a part of quite a few advanced computational methods targeting design and structural analysis, those reported in [68–77] are examples of that, and turbine blades and heart valves are among the examples.

In IGA discretization, specifying Dirichlet boundary conditions could be challenging. That is because the basis functions are generally not interpolatory. In the case of differential equations allowing Dirichlet conditions also on the derivatives, specifying conditions on the derivatives could be easier in IGA discretization than it is in finite element discretization. For example, specifying the slope can be accomplished by constraining the motion of the nearest interior point to the horizontal line passing through the boundary point.

Our objective in the work presented here is to address a related challenge. That is, computational structural analysis where structures with different parametric dimensions are connected with continuity and smoothness. In structural analysis of a membrane and cable, for example, connecting the two with C^0 or C^1 continuity involves challenges similar to those associated with specifying Dirichlet boundary conditions in IGA discretization. Even if the two structures have the same parametric dimensions, connecting them with C^1 continuity could still be challenging.

There has been some earlier related work. They include the bending-strip method for shell–shell [78] and shell–beam [79] structures, where the beam is actually a bending-stabilized cable, penalty formulation [80], and techniques based on Nitsche's method [81]. They also include using extra mesh refinement along the membrane edge [45] to attain C^0 continuity in both the edge direction and the other direction. Using T-splines [82] to attain C^1 continuity when the two structures have the same parametric dimensions is also among the earlier related work.

In our work here, we derive the basis functions that give us the desired smoothness between structures with 2D and 1D parametric dimensions. The derivation involves proper selection of a scale factor for the knot vector of the 1D structure and results in new control-point locations. While our method description will focus on C^0 and C^1 continuity, paths to higher-order continuity will be marked where needed. In presenting the method and its implementation, we will refer to the 2D structure as "membrane" and the 1D structure as "cable." The method and its implementation will, of course, be applicable also to other 2D–1D cases, such as shell–cable and shell–beam structures. When the membrane and cable are connected with smoothness, the strain and rotational freedoms are transferred between the two structures. For easy and efficient implementation of the method, we introduce the Bézier extraction row operators to be used in obtaining the basis functions.

As the limitations of the method we will be presenting, we can mention two points. The smoothness can only be achieved along the cable and its parametric-line continuation in the membrane. The starting membrane and cable meshes need to meet some additional requirements if they are to be connected with a continuity higher than C^1.

We present test computations not only for membrane–cable structures but also for shell–cable structures. We use four structure models: membrane–cable, membrane–bending-stabilized-cable, shell–cable, and shell–bending-stabilized-cable. We use meshes with C^0 continuity and C^2 continuity. In total, we compute eight test cases.

In Sect. 2, we introduce the method for connecting a membrane and cable by T-splines. The test computations are presented in Sect. 3, and the concluding remarks are given in Sect. 4. In Appendix A, we provide the details on the mesh examples, and in Appendix B, we give the derivation of the smoothness constraints used in the method.

2 Connecting a membrane and cable by T-splines

In IGA, connecting a 1D structure, such as a cable, to a 2D structure, such as a membrane, is not that straightforward. For example, in [45], in connecting the cables to the ram-air parachute, extra mesh refinement was used along the membrane edge to attain C^0 continuity in both the edge direction and the other direction. The extra refinement, because of the

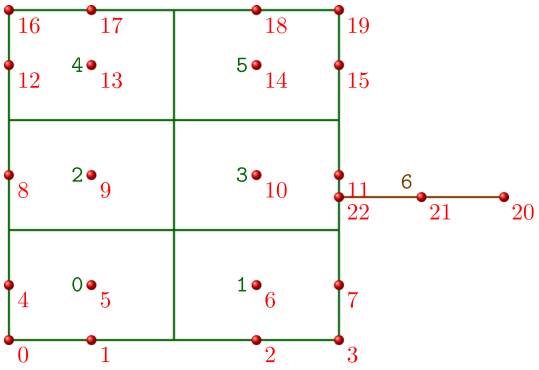

Fig. 1 The membrane and cable elements before connecting them. The *red* circles represent the control points. Each area enclosed by *green* lines represents an element, and it is labeled with a *green* number. The *brown* line represents a cable element, and it is labeled with a *brown* number. In all elements, the local parametric coordinates are defined from left to right in the first direction and from bottom to top (for membrane only) in the second direction. (Color figure online)

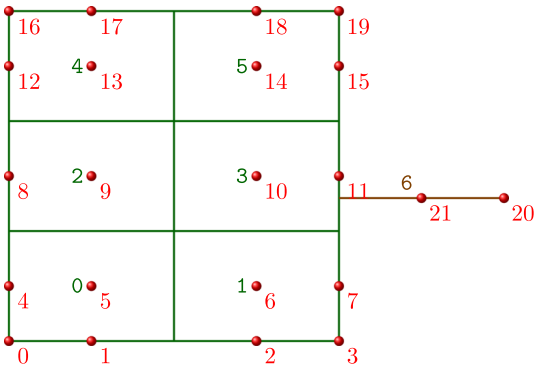

Fig. 2 The membrane and cable elements after connecting them

knot insertion, reduces not only the computational efficiency but also the continuity. Especially with isogeometric shells and bending-stabilized cables [79], the continuity is essential. Here we describe methods to connect a cable to a membrane at any location along its edge, and we also describe methods to attain smoothness along the cable and its parametric-line continuation in the membrane.

2.1 Connecting the cable to the membrane

We assume that the membrane is of rectangular shape. For illustration purposes, it is made of 2×3 quadratic B-spline elements, and the cable consists of one quadratic B-spline element. Figure 1 shows the membrane and cable (for more details on the mesh, see Appendix A.1), and Fig. 2 shows the mesh after connecting them (for more details on the mesh, see Appendix A.2). We will explain how we obtain this mesh.

We represent the local basis functions in the parametric space $-1 \leq \xi^\alpha \leq 1$, where $\alpha = 1, \ldots, n_{\text{pd}}$, and n_{pd} is the number of parametric dimensions. For a global basis function index a or b in element e, we denote the local basis functions as $M_a^e(\xi^1, \xi^2)$ for the membrane elements and as $L_b^e(\xi^1)$ for the cable elements. They are expressed as

$$M_a^e(\xi^1, \xi^2) = N_{a^1}^{e,1}(\xi^1) N_{a^2}^{e,2}(\xi^2) \tag{1}$$

and

$$L_b^e(\xi^1) = N_{b^1}^{e,1}(\xi^1), \tag{2}$$

with the index mapping $e, a \rightarrow (a^1(e,a),\ a^2(e,a))$ and $e, b \rightarrow b^1(e,b)$, and we are dropping "$(e,a)$" and "$(e,b)$" not to crowd the notation. Here, $N_k^{e,\alpha}$ represent 1D functions identified by element number e, direction α, and local index k. Although it is not included, the polynomial order is assumed to be $p = p^{e,\alpha}$, and we may omit the superscripts for notational convenience. The index a^α denotes the local index in α direction, and there is no unique mapping from a^α to a. In fact, quite often, a^α corresponds to multiple a. The symbols $\mathcal{M}^e$ and $\mathcal{L}^e$ represent, for the membrane and cable, the sets of functions with nonzero value in element e.

Remark 1 All the T-splines used in this article can be expressed in this product form. Therefore, Eq. (1) is applicable even after connecting the cable to the membrane. Some of the notation may not be general enough as in NURBS, but they should be straightforward. We are giving up some generality so that we do not further complicate the notation.

Referring to Fig. 1, we are connecting the cable end point with $\xi^1 = \xi_{\text{c}}^{B,1} = -1$ in element $B = 6$ to the membrane edge point with $\xi^1 = \xi_{\text{c}}^{A,1} = 1$ and $\xi^2 = \xi_{\text{c}}^{A,2}$ in element $A = 3$. In those membrane and cable elements, the connection point $\mathbf{x}_{\text{c}}$ can be represented as

$$\left(\mathbf{x}_{\text{c}}^h\right)_M = \sum_{a \in \mathcal{M}^A} \mathbf{x}_a M_a^A(\xi_{\text{c}}^{A,1}, \xi_{\text{c}}^{A,2}) \tag{3}$$

and

$$\left(\mathbf{x}_{\text{c}}^h\right)_L = \sum_{b \in \mathcal{L}^B} \mathbf{x}_b L_b^B(\xi_{\text{c}}^{B,1}). \tag{4}$$

Remark 2 Depending on the parametrization, i) one of $\xi_{\text{c}}^{A,\alpha}$ is either -1 or 1, and ii) $\xi^{B,1}$ is either -1 or 1.

We note that $N_{a^1}^{A,1}(\xi_{\text{c}}^{A,1})$ is either 1 or 0 at the membrane edge. We define the set of functions with value 1 at the membrane edge as $\mathcal{M}_{\text{c}}^A = \left\{ a \in \mathcal{M}^A \middle| N_{a^1}^{A,1}(\xi_{\text{c}}^{A,1}) = 1 \right\}$. With that, the connection point as represented by the membrane becomes

$$\left(\mathbf{x}_{\text{c}}^h\right)_M = \sum_{a \in \mathcal{M}_{\text{c}}^A} \mathbf{x}_a N_{a^2}^{A,2}(\xi_{\text{c}}^{A,2}). \tag{5}$$

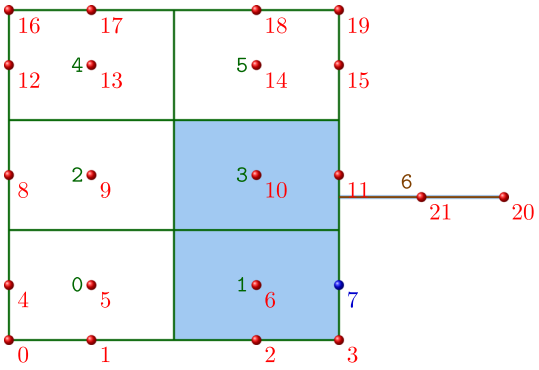

Fig. 3 The elements that the global basis function 7 is contributing to. The *blue* shading and *blue* highlight indicate those elements. (Color figure online)

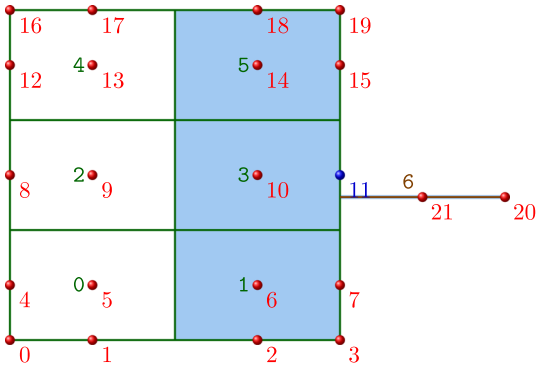

Fig. 4 The elements that the global basis function 11 is contributing to. The *blue* shading and *blue* highlight indicate those elements . (Color figure online)

Similarly, at the cable end, $N_{b^1}^{B,1}(\xi_{\mathrm{c}}^{B,1})$ is either 1 or 0, and, in fact, there is only one function that has value 1, and that is $b^1 = c$. With that, the connection point as represented by the cable becomes

$$\left(\mathbf{x}_{\mathrm{c}}^{h}\right)_{L} = \mathbf{x}_{c}. \tag{6}$$

To connect the membrane and cable, we need $\left(\mathbf{x}_{\mathrm{c}}^{h}\right)_{M} = \left(\mathbf{x}_{\mathrm{c}}^{h}\right)_{L}$, and this can be enforced at the basis-function level. For that, we first exclude the basis function and control point associated with c from the cable element (and actually from the mesh). Then, we add control points $\mathbf{x}_{\overline{a}}$, where $\overline{a} \in \mathcal{M}_{\mathrm{c}}^{A}$, to the cable element. The corresponding basis functions, indexed by $\overline{b} = \overline{a}$, are

$$\overline{L}_{\overline{b}}^{B}(\xi^1) = N_{a^2}^{A,2}(\xi_{\mathrm{c}}^{A,2}) N_{c}^{B,1}(\xi^1), \tag{7}$$

and the overbar is for distinguishing between the basis functions before and after connecting the cable to the membrane. With that, the cable end is always on the membrane edge. The number of functions in the cable element becomes $\left|\mathcal{L}^{B}\right| - 1 + \left|\mathcal{M}_{\mathrm{c}}^{A}\right|$, where $|\mathcal{X}|$ represents the cardinality of a set $\mathcal{X}$.

Figures 3, 4 and 5 illustrate how the basis functions corresponding to the three control points on the membrane edge contribute to the membrane and cable elements. The figures are for 7, 11, and 15, the three control points in $\mathcal{M}_{c}^{A}$. The basis function 22 is removed from the cable and represented by 7, 11,and 15. With that, the modified cable element consists of functions 7, 11, 15, 20, and 21.

Remark 3 The control points 7, 11, and 15 are distinct because of the membrane.

Remark 4 If the membrane and cable had rotational freedoms, they would not be transferred between the two.

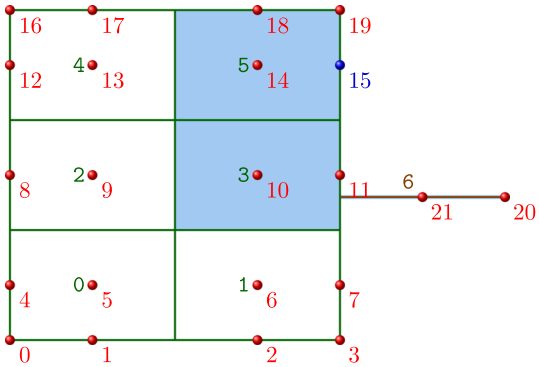

Fig. 5 The elements that the global basis function 15 is contributing to. The *blue* shading and *blue* highlight indicate those elements. (Color figure online)

Remark 5 By generalizing Eq. (5), the method discussed so far can be extended to cases where the connection point is not on the membrane edge but anywhere in the interior.

2.2 Representation of the connected cable with Bézier extraction operators

We now describe how connecting the cable is implemented by using Bézier extraction operators (see the notation in [83, 84]). A basis function of order p can be represented with Bernstein polynomials B_b^p, which are expressed as

$$B_k^p(\xi) = \binom{p}{k} 2^{-p} (1+\xi)^k (1-\xi)^{p-k}, \tag{8}$$

where $k = 0, \ldots, p$, and $\binom{p}{k} = \frac{k!}{k!(p-k)!}$ are the binomial coefficients. The representation of the 1D basis functions we have in Eqs. (1) and (2) will then be in the form

$$N_l^{A,\alpha}(\xi) = \sum_{k=0}^{p^{A,\alpha}} C_{lk}^{A,\alpha} B_k^{p^{A,\alpha}}(\xi) \tag{9}$$

for $l = 0, \ldots, p$. The set of coefficient matrices $\mathbf{C}^{A,\alpha} = \left[C^{A,\alpha}_{lk}\right] \in \mathbb{R}^{(p^{A,\alpha}+1)\times(p^{A,\alpha}+1)}$ are the Bézier extraction operators. However, in a T-spline element, the number of unique $N^{A,\alpha}$ functions may not be equal to $p^{A,\alpha}+1$, and the order of the rows has no significance. Therefore, we represent the Bézier extraction operator as a set of row operators, denoted by $\mathbf{C}^{A,\alpha}_{l} \in \mathbb{R}^{1\times(p^{A,\alpha}+1)}$, with l being the index that identifies the unique function number in an element A, in direction α.

With that, the membrane local basis functions can now be expressed as

$$M^A_a(\xi^1,\xi^2) = \left(\sum_{k=0}^{p^{A,1}} C^{A,1}_{a^1k} B^{p^{A,1}}_k(\xi^1)\right)\left(\sum_{k=0}^{p^{A,2}} C^{A,2}_{a^2k} B^{p^{A,2}}_k(\xi^2)\right), \tag{10}$$

and the cable local basis functions can be expressed as

$$L^B_b(\xi^1) = \sum_{k=0}^{p^{B,1}} C^{B,1}_{b^1k} B^{p^{B,1}}_k(\xi^1). \tag{11}$$

From that and Eq. (2), Eq. (7) can be written as

$$\overline{L}^B_{\overline{b}}(\xi^1) = \underbrace{\left(\sum_{l=0}^{p^{A,2}} C^{A,2}_{a^2l} B^{p^{A,2}}_l(\xi^{A,2}_{\mathrm{c}})\right)}_{\text{scalar}}\left(\sum_{k=0}^{p^{B,1}} C^{B,1}_{ck} B^{p^{B,1}}_k(\xi^1)\right). \tag{12}$$

The scalar term can be expressed in a matrix form. For that, we first define a column matrix with the evaluated Bézier functions as its components:

$$\mathbf{B}^{p^{A,2}}_{\mathrm{c}} = \left[B^{p^{A,2}}_l(\xi^{A,2}_{\mathrm{c}})\right] \in \mathbb{R}^{p^{A,2}+1}. \tag{13}$$

Then the scalar is written as

$$\sum_{l=0}^{p^{A,2}} C^{A,2}_{a^2l} B^{p^{A,2}}_l(\xi^{A,2}_{\mathrm{c}}) = \mathbf{C}^{A,2}_{a^2}\mathbf{B}^{p^{A,2}}_{\mathrm{c}}. \tag{14}$$

We note that this scalar depends on a^2. With that, the Bézier extraction operator $\overline{\mathbf{C}}^{B,1}_{\overline{b}}$ associated with Eq. (12) becomes

$$\overline{\mathbf{C}}^{B,1}_{\overline{b}^1} = \mathbf{C}^{A,2}_{a^2}\mathbf{B}^{p^{A,2}}_{\mathrm{c}}\,\mathbf{C}^{B,1}_{c}. \tag{15}$$

Now, for the examples in Figs. 1 and 2, we express the Bézier extraction row operators for the cable element. The original cable element has

$$\boldsymbol{C}^{6,1}_{22^1} = \begin{bmatrix}1 & 0 & 0\end{bmatrix}, \tag{16}$$

$$\boldsymbol{C}^{6,1}_{21^1} = \begin{bmatrix}0 & 1 & 0\end{bmatrix}, \tag{17}$$

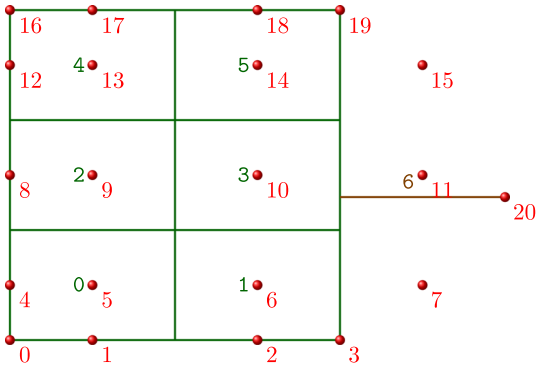

Fig. 6 The membrane and cable elements with C^1 continuity along the cable line

$$\boldsymbol{C}^{6,1}_{20^1} = \begin{bmatrix}0 & 0 & 1\end{bmatrix}. \tag{18}$$

After the connection, we have

$$\overline{\boldsymbol{C}}^{6,1}_{7^1} = 0.245\begin{bmatrix}1 & 0 & 0\end{bmatrix}, \tag{19}$$

$$\overline{\boldsymbol{C}}^{6,1}_{11^1} = 0.710\begin{bmatrix}1 & 0 & 0\end{bmatrix}, \tag{20}$$

$$\overline{\boldsymbol{C}}^{6,1}_{15^1} = 0.045\begin{bmatrix}1 & 0 & 0\end{bmatrix}, \tag{21}$$

$$\overline{\boldsymbol{C}}^{6,1}_{21^1} = \begin{bmatrix}0 & 1 & 0\end{bmatrix}, \tag{22}$$

$$\overline{\boldsymbol{C}}^{6,1}_{20^1} = \begin{bmatrix}0 & 0 & 1\end{bmatrix}. \tag{23}$$

Remark 6 The scalars seen in front of the row operators in Eqs. (19)–(21) can be calculated from Eq. (14).

2.3 Connecting the membrane and cable with smoothness

The smoothness can play a role if the bending stiffness of the cable will influence the membrane structure. For that purpose, we describe the case with higher-order continuity in the cable direction at the connection point. In this method, the smoothness is along the cable and its parametric-line continuation in the membrane. Again, we use Fig. 1 as an example, and Fig. 6 shows the mesh after connecting the cable and membrane with C^1 continuity along the cable line (for more details on the mesh, see Appendix A.3). The smoothness is along the cable and the parametric line $\xi^2 = \xi^{A,2}_{\mathrm{c}}$ in the membrane element. We use the knot removal technique to have the desired continuity in the function space. We will next explain the process.

In the B-spline mesh (Fig. 1), the basis functions $N^{A,1}_{a^1}$ for $a \in \mathcal{M}^A_{\mathrm{c}}$ are the same. In other words, $a = 7$, 11, and 15 are pointing to the same index a^1. Moreover, $a = 6$, 10, and 14 are pointing to a common index a^1, and $a = 5$, 9, and 13 are pointing to a common index a^1. We group them as $\mathcal{M}^A_{\mathrm{c1}}$ and

$\mathcal{M}^A_{c0}$. The position along the parametric line is expressed as

$$\mathbf{x}(\xi^1, \xi^{A,2}) = \sum_{a\in\mathcal{M}^A_{c0}} \mathbf{x}_a M^A_a(\xi^1, \xi^{A,2}_c) + \sum_{a\in\mathcal{M}^A_{c1}} \mathbf{x}_a M^A_a(\xi^1, \xi^{A,2}_c) + \sum_{a\in\mathcal{M}^A_{c}} \mathbf{x}_a M^A_a(\xi^1, \xi^{A,2}_c). \tag{24}$$

We know that

$$\sum_{a\in\mathcal{M}^A_{c0}} N^{A,2}_{a^2}(\xi^{A,2}_c) = 1, \tag{25}$$

$$\sum_{a\in\mathcal{M}^A_{c1}} N^{A,2}_{a^2}(\xi^{A,2}_c) = 1, \tag{26}$$

$$\sum_{a\in\mathcal{M}^A_{c}} N^{A,2}_{a^2}(\xi^{A,2}_c) = 1. \tag{27}$$

From Eqs. (24)–(27), we observe the apparent directional basis functions and control points along the parametric line to be

$$\tilde{M}^A_0(\xi^1) = \sum_{a\in\mathcal{M}^A_{c0}} M^A_a(\xi^1, \xi^{A,2}_c) \tag{28}$$

$$= N^{A,1}_{a^1}(\xi^1), \tag{29}$$

$$\tilde{M}^A_1(\xi^1) = \sum_{a\in\mathcal{M}^A_{c1}} M^A_a(\xi^1, \xi^{A,2}_c) \tag{30}$$

$$= N^{A,1}_{a^1}(\xi^1), \tag{31}$$

$$\tilde{M}^A_2(\xi^1) = \sum_{a\in\mathcal{M}^A_{c}} M^A_a(\xi^1, \xi^{A,2}_c) \tag{32}$$

$$= N^{A,1}_{a^1}(\xi^1) \tag{33}$$

and

$$\tilde{\mathbf{x}}^A_0 = \sum_{a\in\mathcal{M}^A_{c0}} \mathbf{x}_a N^{A,2}_{a^2}(\xi^2_c), \tag{34}$$

$$\tilde{\mathbf{x}}^A_1 = \sum_{a\in\mathcal{M}^A_{c1}} \mathbf{x}_a N^{A,2}_{a^2}(\xi^2_c), \tag{35}$$

$$\tilde{\mathbf{x}}^A_2 = \sum_{a\in\mathcal{M}^A_{c}} \mathbf{x}_a N^{A,2}_{a^2}(\xi^2_c). \tag{36}$$

Similar observations can be made for the adjacent element 2. For notational convenience, we map the control points of the cable as

$$\mathbf{x}^B_0 = \mathbf{x}_{22}, \tag{37}$$

$$\mathbf{x}^B_1 = \mathbf{x}_{21}, \tag{38}$$

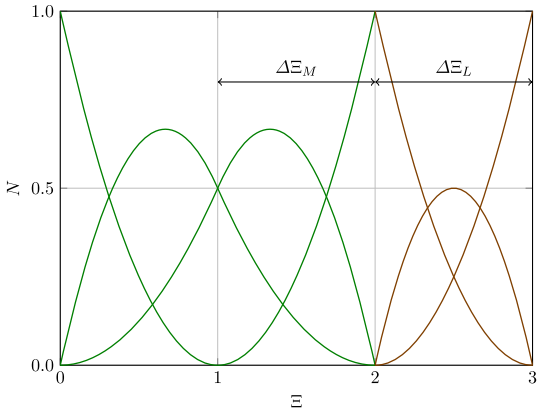

Fig. 7 Apparent basis functions in the 1D representation along the cable line. The *green* ones are for the membrane, and the *brown* ones are for the cable. $\Delta\Xi_M$ and $\Delta\Xi_L$ mark the neighboring nonzero knot spans of the membrane and cable. (Color figure online)

$$\mathbf{x}^B_2 = \mathbf{x}_{20}. \tag{39}$$

Figure 7 shows the apparent basis functions. These basis functions can be identified by the knot vector $\boldsymbol{\Xi} = \{0, 0, 0, 1, 2, 2, 2, 3, 3, 3\}$, with $0 \le \Xi \le 2$ for the membrane and $2 \le \Xi \le 3$ for the cable.

Remark 7 The linear transformation of the knot vector values does not change the basis functions. When we connect two patches, a linear transformation can be applied in each patch. For example, if we scale the knots for the cable by a factor 0.5, we get $\boldsymbol{\Xi} = \{0, 0, 0, 1, 2, 2, 2, 2.5, 2.5, 2.5\}$. Although the parametric space would be different, this would not change the element-wise functions and would not influence the discretization. However, the choice of the scale factor influences how the cable and membrane are connected. In fact, the desired smoothness can only be achieved with the correct scale factor. We will explain this more in Remark 8, after explaining the procedure for connecting the cable and membrane.

Figure 8 shows the functions after the first and second knot removals at $\Xi = 2$. At each knot removal, one basis function vanishes, which means that the corresponding control point is removed. It is assumed that the geometry will not change after the knot removals. Therefore, the following relationship holds in each element:

$$\sum_{k=0}^{p} N_k \mathbf{x}_k = \sum_{k=0}^{p} \overline{N}_k \overline{\mathbf{x}}_k, \tag{40}$$

where k is the element-wise index, and N_k and $\overline{N}_k$ are the directional basis functions before and after the knot removals. Using the Bézier extraction operators, we can rewrite Eq. (40)

as

$$\sum_{k=0}^{p}\sum_{l=0}^{p}\mathbf{x}_k C_{kl} B_l = \sum_{k=0}^{p}\sum_{l=0}^{p}\overline{\mathbf{x}}_k \overline{C}_{kl} B_l. \tag{41}$$

Because B_l are linearly independent, we obtain the following relationship for $l = 0, \ldots, p$:

$$\overline{\mathbf{x}}_k = \sum_{l=0}^{p}\mathbf{x}_l \left[\mathsf{C}\left(\overline{\mathsf{C}}\right)^{-1}\right]_{lk}. \tag{42}$$

For notational convenience, we rearrange this as

$$\overline{\mathbf{x}}_k = \sum_{l=0}^{p}\left[\left(\overline{\mathsf{C}}\right)^{-\mathsf{T}}\mathsf{C}^{\mathsf{T}}\right]_{kl}\mathbf{x}_l. \tag{43}$$

Figure 9 shows an example of the context for Eq. (43) in control-point conversions for an element. The example is based on

$$\mathsf{C} = \begin{bmatrix} \frac{1}{2} & 0 & 0 \\ \frac{1}{2} & 1 & 0 \\ 0 & 0 & 1 \end{bmatrix} \tag{44}$$

and

$$\overline{\mathsf{C}} = \begin{bmatrix} \frac{1}{2} & 0 & 0 \\ \frac{1}{2} & 1 & \frac{1}{2} \\ 0 & 0 & \frac{1}{2} \end{bmatrix}. \tag{45}$$

The continuity desired after the second knot removal can be expressed by the equations

$$\tilde{\overline{\mathbf{x}}}_1^A = \overline{\mathbf{x}}_0^B, \tag{46}$$

$$\tilde{\overline{\mathbf{x}}}_2^A = \overline{\mathbf{x}}_1^B. \tag{47}$$

We note that A and B are the elements in the membrane and the cable, and those positions are calculated from Eq. (43) for the membrane and cable elements. Figure 10 shows an example of the conversions for both the membrane and cable elements.

Remark 8 As explained in Remark 7, the scale factor for the cable knot vector influences how the cable and membrane are connected, and the desired smoothness can only be achieved with the correct factor. Different scale factors give different $\tilde{\overline{\mathbf{x}}}_2^A$. For $p = 2$, Eqs. (46) and (47) translate to

$$\tilde{\mathbf{x}}_2^A = \mathbf{x}_0^B, \tag{48}$$

$$\tilde{\mathbf{x}}_2^A = \frac{s\tilde{\mathbf{x}}_1^A + \mathbf{x}_1^B}{s+1}, \tag{49}$$

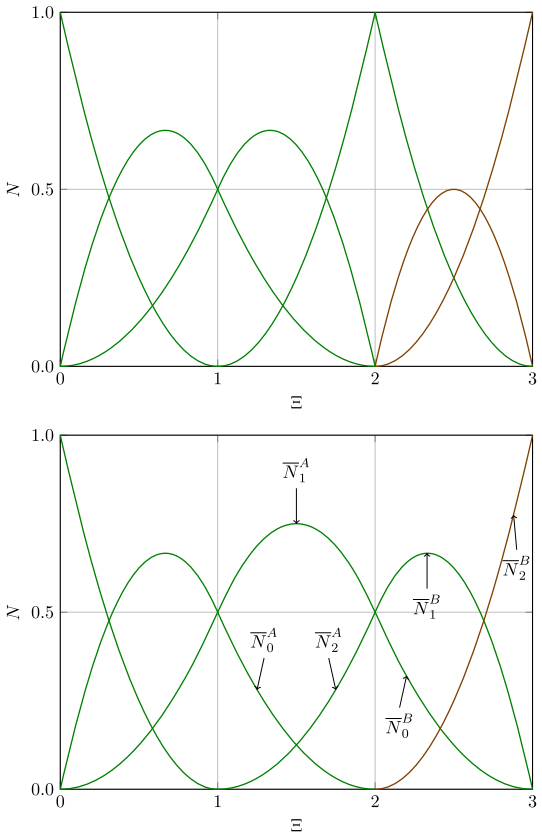

Fig. 8 Apparent basis functions in the 1D representation along the cable line. After the first (*top*) and second (*bottom*) knot removals

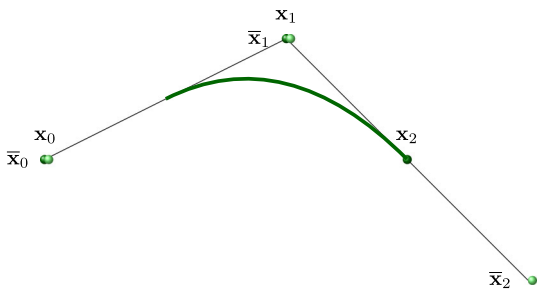

Fig. 9 An example of the context for Eq. (43) in control-point conversions for an element. The curve (thick *green* line) and control points (*dark green* circles), and the control points obtained with Eq. (43) (*light green* circles). (Color figure online)

where s is the ratio of the neighboring nonzero knot spans of the cable ($\Delta\Xi_L$) and membrane ($\Delta\Xi_M$):

$$s = \frac{\Delta\Xi_L}{\Delta\Xi_M}. \tag{50}$$

The derivation can be found in Appendix B. With Eq. (49), we select s. In the example of Fig. 1, that gives us $s = 1$.

Remark 9 To have the highest continuity in using B-splines with polynomial order p, we need to satisfy p conditions

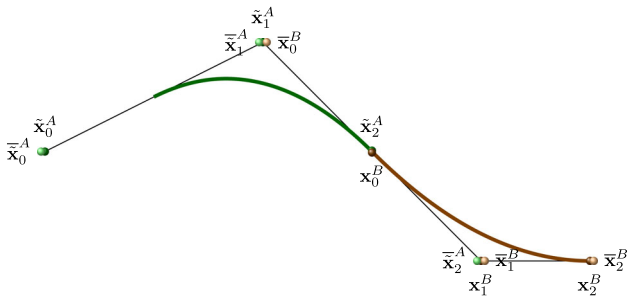

Fig. 10 An example of the context for Eq. (43) in control-point conversions for both the membrane and cable elements. The membrane (thick *green* curve) and the apparent control points (*dark green* circles). The cable (thick *brown* curve) and the control points (*dark brown* circles). The control points after the conversions are *light green* circles (membrane) and *light brown* circles (cable). If Eqs. (46) and (47) are satisfied after the conversions, the curve will have the desired continuity and the two knots can be removed without changing the geometry

that are generalization of those in Eqs. (46) and (47). The conditions are

$$\bar{\tilde{\mathbf{x}}}_k^A = \bar{\mathbf{x}}_{k-1}^B, \tag{51}$$

for $k = 1, \ldots, p$.

Then, we remove the control points 22 and 21. The new positions of the control points 7, 11, 15, 6, 10, and 14 are obtained from Eq. (43). With the basis functions corresponding to those, we can form the basis functions in the cable element. This can be done in the same way we did in connecting the cable and membrane with C^0 continuity. The corresponding basis functions, indexed by $\bar{b} = \bar{a} \in \mathcal{M}_{\mathrm{c1}}^A \cup \mathcal{M}_{\mathrm{c}}^A$, are

$$\bar{L}_{\bar{b}}^B(\xi^1) = \bar{N}_{a^2}^{A,2}(\xi_{\mathrm{c}})\bar{N}_{\bar{b}^1}^{B,1}(\xi^1). \tag{52}$$

The control points and Bézier extraction operators for the membrane elements also change. We provide the Bézier extraction operators in Appendix A.3, and Eq. (43) can be used for obtaining $\bar{\mathbf{x}}_{\bar{a}}^A$, where $\bar{a} \in \mathcal{M}_{\mathrm{c1}}^A \cup \mathcal{M}_{\mathrm{c}}^A$.

Figures 11, 12, 13, 14, 15 and 16 illustrate how the basis functions in $\mathcal{M}_{\mathrm{c1}}^A$ and $\mathcal{M}_{\mathrm{c}}^A$ contribute to the membrane and cable elements. The figures are for 7, 11, and 15, the three control points in $\mathcal{M}_{c}^A$, and 6, 10, and 14, the three control points in $\mathcal{M}_{c1}^A$. As mentioned earlier, the basis functions 22 and 21 are removed from the cable. The new cable element consists of the basis functions 6, 10, 14, 7, 11, 15, and 20, and we can see the first three as replacements for 22, and the second three as replacements for 21.

Remark 10 In the membrane, up to $(2p+1)\times(p-1)$ elements need to be modified, $(2p+1)$ in the edge direction, and $(p-1)$ in the other direction. In the cable, up to p elements neighboring the membrane need to be modified.

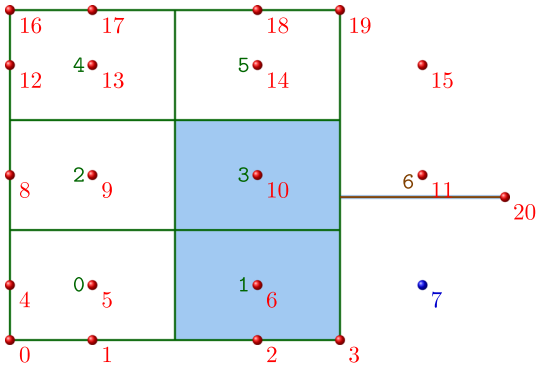

Fig. 11 The elements that the global basis function 7 is contributing to. The *blue* shading and *blue* highlight indicate those elements. (Color figure online)

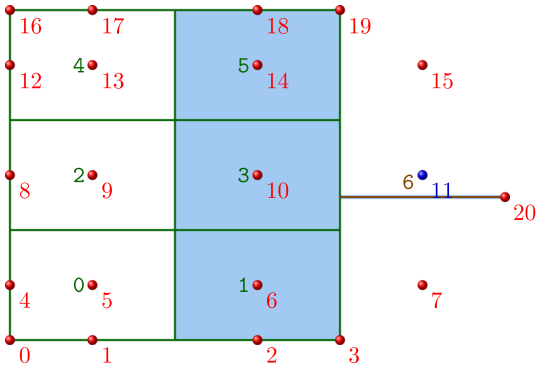

Fig. 12 The elements that the global basis function 11 is contributing to. The *blue* shading and *blue* highlight indicate those elements. (Color figure online)

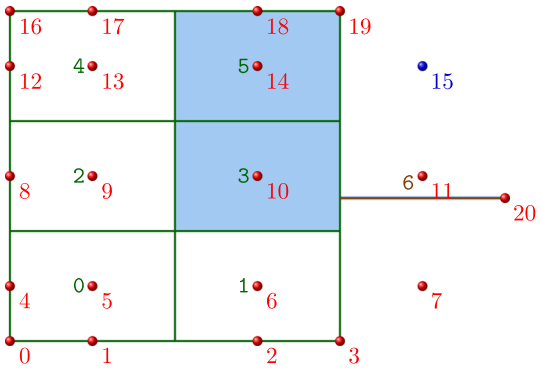

Fig. 13 The elements that the global basis function 15 is contributing to. The *blue* shading and *blue* highlight indicate those elements. (Color figure online)

Remark 11 The control points 7, 11, and 15 are distinct because of the membrane.

Remark 12 The strain and rotational freedoms are transferred between the two structures. Even if they are not based on a shell model or bending-stabilized cable, this smoothness requirement would add some kind of bending effect to the

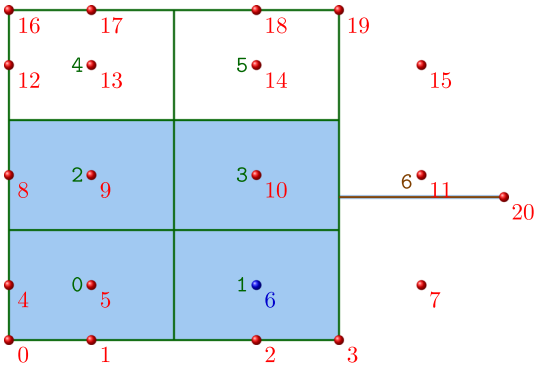

Fig. 14 The elements that the global basis function 6 is contributing to. The *blue* shading and *blue* highlight indicate those elements. (Color figure online)

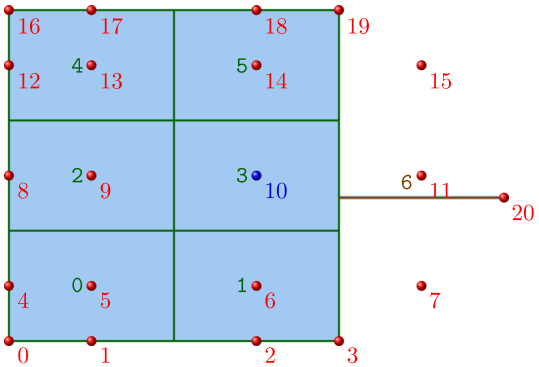

Fig. 15 The elements that the global basis function 10 is contributing to. The *blue* shading and *blue* highlight indicate those elements. (Color figure online)

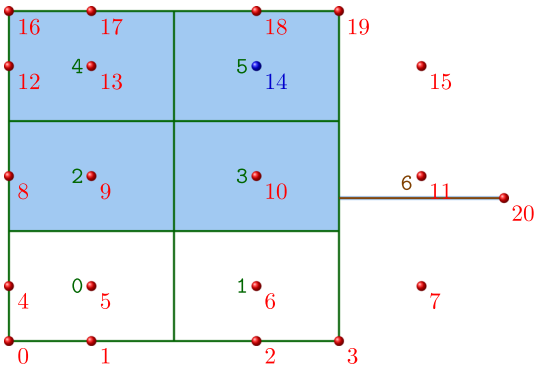

Fig. 16 The elements that the global basis function 14 is contributing to. The *blue* shading and *blue* highlight indicate those elements. (Color figure online)

solution, which will be smaller and smaller with mesh refinement.

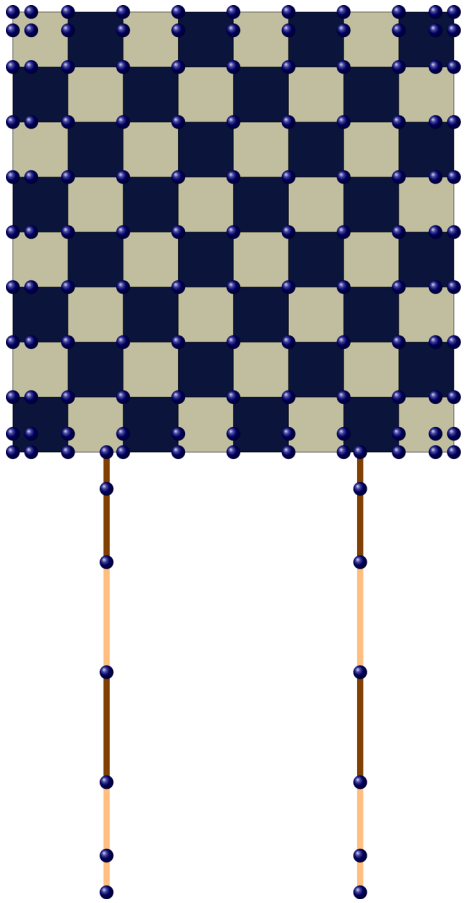

Fig. 17 The membrane and cable meshes before connecting them. The checkerboard pattern and alternating colors are for differentiating between the elements, and circles represent the control points

3 Test computations

We use four structure models: membrane–cable, membrane–bending-stabilized-cable, shell–cable, and shell–bending-stabilized-cable. We use meshes with C^0 and C^2 continuity between the membrane and cable. In total, we compute eight test cases. The membrane does not have bending stiffness; the shell does. The membrane includes a wrinkling model [85]. The shell model is from [66]. The cable includes a slacking model, which precludes compression. The bending-stabilized cable is based on the model in [79], where the bending stress is represented by the second area moment and the curvature.

3.1 Problem setup

Figure 17 shows the mesh before connecting the membrane and cable. The material properties for the membrane, shell, cable, and bending-stabilized cable are shown in Tables 1 and 2. The meshes with C^0 and C^2 continuity between the membrane and cable will be called "C^0 Mesh" and "C^2 Mesh."

Table 1 Material properties for the membrane and shell. Young's modulus E, thickness h_{th}, density ρ, and Poisson's ratio ν

	Eh_{th} (N/m)	ρh_{th} (kg/m^2)	ν (–)	h_{th} (mm)
Membrane	30,000	0.456	0.3	–
Shell	30,000	0.456	0.3	0.400

Table 2 Material properties for the cable and bending-stabilized cable. Young's modulus E, area A, density ρ, and second area moment I_0

	EA (N)	ρA (kg/m)	EI_0 (N · mm^2)
Cable	48	0.000730	–
Bending-stabilized cable	48	0.000730	2.56

Both are based on cubic B-splines. Figures 18 and 19 show the meshes. We hook the membrane and cables at the two corners and two ends shown in those figures, all at the same elevation. The gravity is 9.81 m/s^2. We gradually shorten the distance between the hooked membrane edge and cable ends from 171 to 85.5 mm by moving the cable ends.

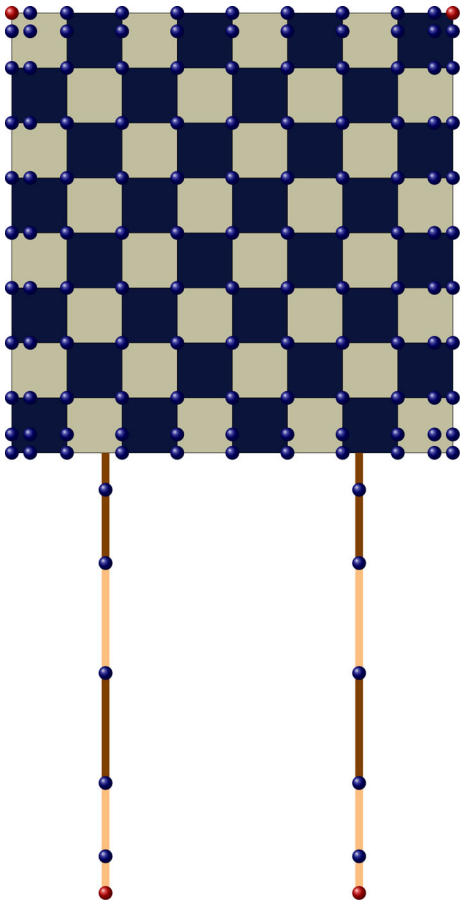

Fig. 18 C^0 Mesh. The checkerboard pattern and alternating colors are for differentiating between the elements, and circles represent the control points. The *red* control points are those with specified position in the computation

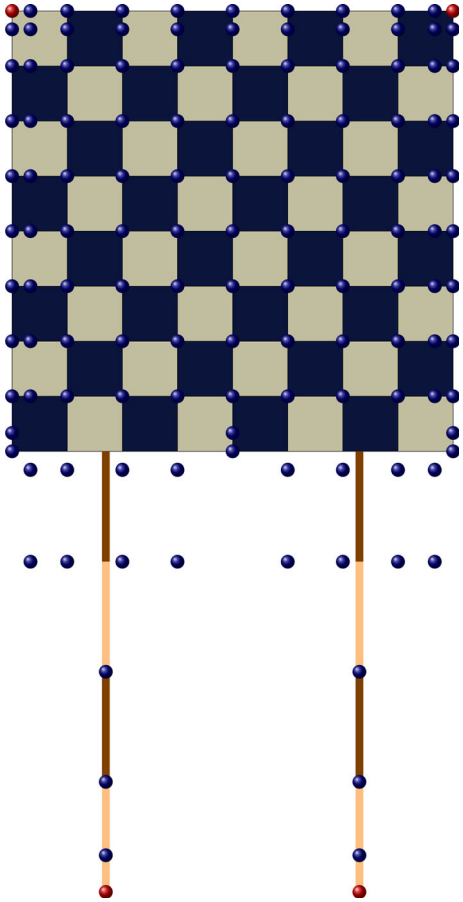

Fig. 19 C^2 Mesh. The checkerboard pattern and alternating colors are for differentiating between the elements, and circles represent the control points. The *red* control points are those with specified position in the computation

Remark 13 To obtain the settled solution in each test case computed, depending on the test case, we either use the steady-state formulation or the unsteady formulation with a relatively large time-step size. The unsteady formulation is used to avoid the matrix singularities associated with slacking.

3.2 Results

Figure 20 shows the settled solution for all eight cases. Looking at the cases with C^0 Mesh, we can clearly see that the rotational freedom is not transferred between the membrane and cables. In the cases with C^2 Mesh, we see smoothness along the 1D structure and its parametric-line continuation in the 2D structure, as expected, even if the 2D structure is membrane or the 1D structure is cable. Naturally, how local the smoothness is in computations with the C^2 Mesh, i.e., how small the radius of curvature is, depends on the element

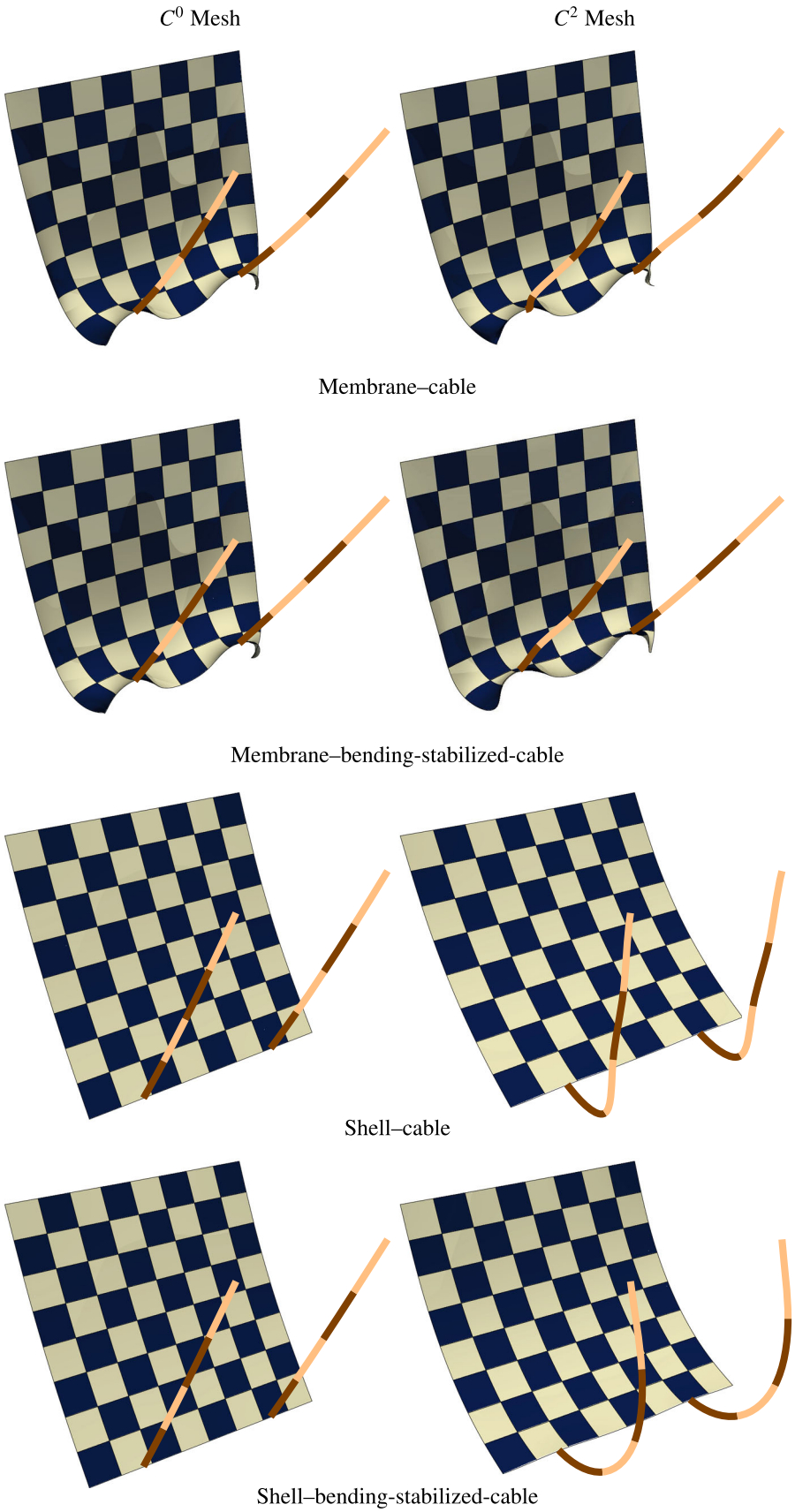

Fig. 20 Settled solution for all eight cases computed

sizes near where the 2D and 1D structures are connected. Therefore, the decision to seek smoothness or just continuity would depend on those element sizes.

4 Concluding remarks

We have presented a T-splines computational method and its implementation for structural analysis where structures with different parametric dimensions are connected with continuity and smoothness. We derived basis functions that give us the desired smoothness between structures with 2D and 1D parametric dimensions. The derivation involves proper selection of a scale factor for the knot vector of the 1D structure and results in new control-point locations. While the method description focused on C^0 and C^1 continuity, paths to higher-order continuity were marked where needed. In presenting the method and its implementation, we referred to the 2D structure as "membrane" and the 1D structure as "cable." The method and its implementation are of course applicable also to other 2D–1D cases, such as shell–cable and shell–beam structures. When the membrane and cable are connected with smoothness, the strain and rotational freedoms are transferred between the two structures. For easy and efficient implementation of the method, we introduced the Bézier extraction row operators used in obtaining the basis functions. We presented test computations for combinations for four structural models and two meshes. The structural models were membrane–cable, membrane–bending-stabilized-cable, shell–cable, and shell–bending-stabilized-cable. The meshes were with C^0 continuity and C^2 continuity. The computations clearly demonstrate how the method performs in the classes of structural mechanics problems targeted.

Acknowledgements This work was supported in part by Grant-in-Aid for Scientific Research (A) 18H04100 from Japan Society for the Promotion of Science, JST-CREST JPMJCR1911, Rice–Waseda research agreement, and International Technology Center Indo-Pacific (ITC IPAC) Contract FA520921C0010. The work was also supported by Grant-in-Aid for Research Activity Start-up 20K22401 and Grant-in-Aid for Early-Career Scientists 22K17903 from Japan Society for the Promotion of Science (first author). The mathematical model and computational method parts of the work were supported in part by ARO Grant W911NF-17-1-0046 and Top Global University Project of Waseda University (third author).

A Examples of meshes

A.1 Before connecting the cable and membrane

The example in Fig. 1 has two quadratic B-spline patches, one for the membrane and one for the cable. The membrane knot vectors in the two directions are $\boldsymbol{\Xi}_M^1 = \{0, 0, 0, 1, 2, 2, 2\}$ and $\boldsymbol{\Xi}_M^2 = \{0, 0, 0, 1, 2, 3, 3, 3\}$. The cable knot vector is $\boldsymbol{\Xi}_L^1 = \{0, 0, 0, 1, 1, 1\}$. Figure 21 shows a mesh with the same basis functions as those in the mesh in Fig. 1. Just the geometry is more complex. We provide in Table 3 the global basis function indices used in each element, and corresponding element-wise indices for the directional basis functions. In Table 4, we provide the Bézier extraction row operators corresponding to those element-wise indices.

A.2 After connecting the cable and membrane with C^0 continuity

Figure 22 shows the mesh obtained by upgrading the mesh in Fig. 21 to C^0 continuity in connecting the membrane and cable. The new mesh is no longer represented by B-splines. We provide in Table 5 the global basis function indices used in each element and the corresponding element-wise indices for the directional basis functions. In Table 6, we provide the Bézier extraction row operators corresponding to those element-wise indices.

A.3 After connecting the cable and membrane with C^1 continuity

Figure 23 shows the mesh obtained by upgrading the mesh in Fig. 21 to C^1 continuity in connecting the membrane and cable. Like the mesh in Fig. 22, it is no longer represented by B-splines. We provide in Table 7 the global basis function

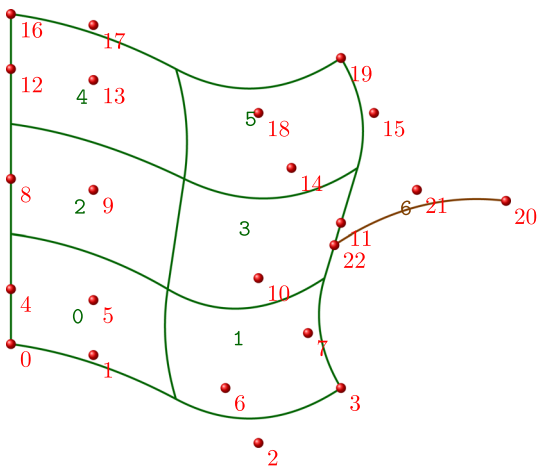

Fig. 21 The membrane and cable elements before connecting them. The basis functions are the same as those in Fig. 1

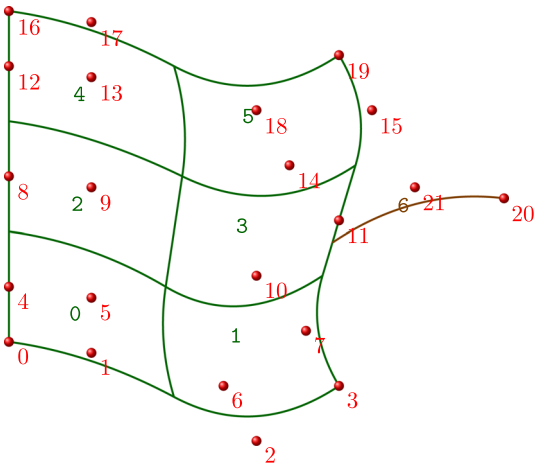

Fig. 22 The membrane and cable elements after connecting them with C^0 continuity. The basis functions are the same as those in Fig. 2

indices used in each element and the corresponding element-wise indices for the directional basis functions. In Table 8, we provide the Bézier extraction row operators corresponding to those element-wise indices.

Table 3 The membrane and cable elements before connecting them. For each element e, the global indices a or b, and their element-wise indices $k = a^1$ and a^2 or $k = b^1$. The corresponding Bézier extraction row operators are provided in Table 4

e	$a \in \mathcal{M}^e$ or $b \in \mathcal{L}^e$									
0	a	0	1	2	4	5	6	8	9	10
	a^1	0	1	2	0	1	2	0	1	2
	a^2	3	3	3	4	4	4	5	5	5
1	a	1	2	3	5	6	7	9	10	11
	a^1	0	1	2	0	1	2	0	1	2
	a^2	3	3	3	4	4	4	5	5	5
2	a	4	5	6	8	9	10	12	13	14
	a^1	0	1	2	0	1	2	0	1	2
	a^2	3	3	3	4	4	4	5	5	5
3	a	5	6	7	9	10	11	13	14	15
	a^1	0	1	2	0	1	2	0	1	2
	a^2	3	3	3	4	4	4	5	5	5
4	a	8	9	10	12	13	14	16	17	18
	a^1	0	1	2	0	1	2	0	1	2
	a^2	3	3	3	4	4	4	5	5	5
5	a	9	10	11	13	14	15	17	18	19
	a^1	0	1	2	0	1	2	0	1	2
	a^2	3	3	3	4	4	4	5	5	5
6	b	22	21	20						
	b^1	0	1	2						

Table 4 The membrane and cable elements before connecting them. For element e and element-wise index k, the Bézier extraction row operator for the directional basis functions

e	α	k	$\mathbf{C}_k^{e,\alpha}$		
0	1	0	1	0	0
		1	0	1	0.5
		2	0	0	0.5
	2	3	1	0	0
		4	0	1	0.5
		5	0	0	0.5
1	1	0	0.5	0	0
		1	0.5	1	0
		2	0	0	1
	2	3	1	0	0
		4	0	1	0.5
		5	0	0	0.5
2	1	0	1	0	0
		1	0	1	0.5
		2	0	0	0.5
	2	3	0.5	0	0
		4	0.5	1	0.5
		5	0	0	0.5
3	1	0	0.5	0	0
		1	0.5	1	0
		2	0	0	1
	2	3	0.5	0	0
		4	0.5	1	0.5
		5	0	0	0.5
4	1	0	1	0	0
		1	0	1	0.5
		2	0	0	0.5
	2	3	0.5	0	0
		4	0.5	1	0
		5	0	0	1
5	1	0	0.5	0	0
		1	0.5	1	0
		2	0	0	1
	2	3	0.5	0	0
		4	0.5	1	0
		5	0	0	1
6	1	0	1	0	0
		1	0	1	0
		2	0	0	1

B Derivation of the smoothness constraints given by Eqs. (48) and (49)

We do the derivation for a general case of the knot removals in connecting a membrane and cable. For $p = 2$, with the knot spans of $\{\Delta\Xi_1, \Delta\Xi_2, \Delta\Xi_3\}$, where $\Delta\Xi_2$ is the knot span for the element in consideration, the Bézier extraction

Table 5 The membrane and cable elements after connecting them with C^0 continuity. For each element e, the global indices a or b, and their element-wise indices $k = a^1$ and a^2 or $k = b^1$. The corresponding Bézier extraction row operators are provided in Table 6

e	$a \in \mathcal{M}^e$ or $b \in \mathcal{L}^e$									
0	a	0	1	2	4	5	6	8	9	10
	a^1	0	1	2	0	1	2	0	1	2
	a^2	3	3	3	4	4	4	5	5	5
1	a	1	2	3	5	6	7	9	10	11
	a^1	0	1	2	0	1	2	0	1	2
	a^2	3	3	3	4	4	4	5	5	5
2	a	4	5	6	8	9	10	12	13	14
	a^1	0	1	2	0	1	2	0	1	2
	a^2	3	3	3	4	4	4	5	5	5
3	a	5	6	7	9	10	11	13	14	15
	a^1	0	1	2	0	1	2	0	1	2
	a^2	3	3	3	4	4	4	5	5	5
4	a	8	9	10	12	13	14	16	17	18
	a^1	0	1	2	0	1	2	0	1	2
	a^2	3	3	3	4	4	4	5	5	5
5	a	9	10	11	13	14	15	17	18	19
	a^1	0	1	2	0	1	2	0	1	2
	a^2	3	3	3	4	4	4	5	5	5
6	b	7	11	15	21	20				
	b^1	0	1	2	3	4				

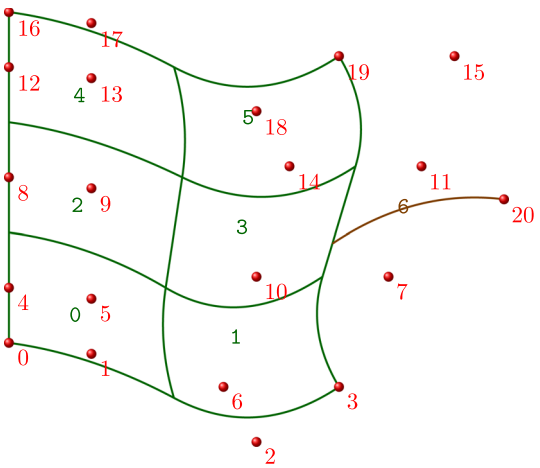

Fig. 23 The membrane and cable elements after connecting them with C^1 continuity. The basis functions are the same as those in Fig. 6

operator can be written as

$$\mathbf{C} = \begin{bmatrix} \frac{\Delta\Xi_2}{\Delta\Xi_1+\Delta\Xi_2} & 0 & 0 \\ \frac{\Delta\Xi_1}{\Delta\Xi_1+\Delta\Xi_2} & 1 & \frac{\Delta\Xi_3}{\Delta\Xi_2+\Delta\Xi_3} \\ 0 & 0 & \frac{\Delta\Xi_2}{\Delta\Xi_2+\Delta\Xi_3} \end{bmatrix}. \tag{53}$$

The membrane knot spans are $\{(\Delta\Xi_M)_1,\ \Delta\Xi_M,\ 0\}$. The last knot span is zero because it is at the end of the patch.

Table 6 The membrane and cable elements after connecting them with C^0 continuity. For element e and element-wise index k, the Bézier extraction row operator for the directional basis functions

e	α	k	$\mathbf{C}_k^{e,\alpha}$		
0	1	0	1	0	0
		1	0	1	0.5
		2	0	0	0.5
	2	3	1	0	0
		4	0	1	0.5
		5	0	0	0.5
1	1	0	0.5	0	0
		1	0.5	1	0
		2	0	0	1
	2	3	1	0	0
		4	0	1	0.5
		5	0	0	0.5
2	1	0	1	0	0
		1	0	1	0.5
		2	0	0	0.5
	2	3	0.5	0	0
		4	0.5	1	0.5
		5	0	0	0.5
3	1	0	0.5	0	0
		1	0.5	1	0
		2	0	0	1
	2	3	0.5	0	0
		4	0.5	1	0.5
		5	0	0	0.5
4	1	0	1	0	0
		1	0	1	0.5
		2	0	0	0.5
	2	3	0.5	0	0
		4	0.5	1	0
		5	0	0	1
5	1	0	0.5	0	0
		1	0.5	1	0
		2	0	0	1
	2	3	0.5	0	0
		4	0.5	1	0
		5	0	0	1
6	1	0	0.245	0	0
		1	0.71	0	0
		2	0.045	0	0
		3	0	1	0
		4	0	0	1

Table 7 The membrane and cable elements after connecting them with C^1 continuity. For each element e, the global indices a or b, and their element-wise indices $k = a^1$ and a^2 or $k = b^1$. The corresponding Bézier extraction row operators are provided in Table 8

e	$a \in \mathcal{M}^e$ or $b \in \mathcal{L}^e$									
0	a	0	1	2	4	5	6	8	9	10
	a^1	3	4	5	0	1	2	0	1	2
	a^2	6	6	6	7	7	7	8	8	8
1	a	1	2	3	5	6	7	9	10	11
	a^1	3	4	5	0	1	2	0	1	2
	a^2	6	6	6	7	7	7	8	8	8
2	a	4	5	6	8	9	10	12	13	14
	a^1	0	1	2	0	1	2	0	1	2
	a^2	3	3	3	4	4	4	5	5	5
3	a	5	6	7	9	10	11	13	14	15
	a^1	0	1	2	0	1	2	0	1	2
	a^2	3	3	3	4	4	4	5	5	5
4	a	8	9	10	12	13	14	16	17	18
	a^1	0	1	2	0	1	2	3	4	5
	a^2	6	6	6	7	7	7	8	8	8
5	a	9	10	11	13	14	15	17	18	19
	a^1	0	1	2	0	1	2	3	4	5
	a^2	6	6	6	7	7	7	8	8	8
6	b	6	10	14	7	11	15	20		
	b^1	0	1	2	3	4	5	6		

With that, from Eq. (53), the Bézier extraction operator for the membrane is expressed as

$$\mathbf{C}^A = \begin{bmatrix} c_1 & 0 & 0 \\ c_2 & 1 & 0 \\ 0 & 0 & 1 \end{bmatrix}, \tag{54}$$

where $c_1 = \frac{\Delta\Xi_M}{(\Delta\Xi)_1+\Delta\Xi_M}$ and $c_2 = 1 - c_1$. For the cable, the knot spans are $\{0,\ \Delta\Xi_L,\ (\Delta\Xi_L)_3\}$, and the Bézier extraction operator is expressed as

$$\mathbf{C}^B = \begin{bmatrix} 1 & 0 & 0 \\ 0 & 1 & c_3 \\ 0 & 0 & c_4 \end{bmatrix}, \tag{55}$$

where $c_4 = \frac{\Delta\Xi_L}{\Delta\Xi_L+(\Delta\Xi_L)_3}$ and $c_3 = 1-c_4$. After the two knot removals, we obtain the following knot spans:

$$\Delta\overline{\boldsymbol{\Xi}} = \{\underbrace{(\Delta\Xi_M)_1,\ \overbrace{\Delta\Xi_M,\ \Delta\Xi_L}^{B},}_{A}\ (\Delta\Xi_L)_3\}. \tag{56}$$

Table 8 The membrane and cable elements after connecting them with C^1 continuity. For element e and element-wise index k, the Bézier extraction row operator for the directional basis functions

e	α	k	$\mathbf{C}_k^{e,\alpha}$		
0	1	0	1	0	0
		1	0	1	0.5
		2	0	0	0.5
		3	1	0	0
		4	0	1	0.5
		5	0	0	0.5
	2	6	1	0	0
		7	0	1	0.5
		8	0	0	0.5
1	1	0	0.5	0	0
		1	0.5	1	0.5
		2	0	0	0.5
		3	0.5	0	0
		4	0.5	1	0
		5	0	0	1
	2	6	1	0	0
		7	0	1	0.5
		8	0	0	0.5
2	1	0	1	0	0
		1	0	1	0.5
		2	0	0	0.5
	2	3	0.5	0	0
		4	0.5	1	0.5
		5	0	0	0.5
3	1	0	0.5	0	0
		1	0.5	1	0.5
		2	0	0	0.5
	2	3	0.5	0	0
		4	0.5	1	0.5
		5	0	0	0.5
4	1	0	1	0	0
		1	0	1	0.5
		2	0	0	0.5
		3	1	0	0
		4	0	1	0.5
		5	0	0	0.5
	2	6	0.5	0	0
		7	0.5	1	0
		8	0	0	1
5	1	0	0.5	0	0
		1	0.5	1	0.5
		2	0	0	0.5
		3	0.5	0	0
		4	0.5	1	0
		5	0	0	1
	2	6	0.5	0	0
		7	0.5	1	0
		8	0	0	1
6	1	0	0.1225	0	0
		1	0.355	0	0
		2	0.0225	0	0
		3	0.1225	0.245	0
		4	0.355	0.71	0
		5	0.0225	0.045	0
		6	0	0	1

This gives

$$\bar{\mathbf{C}}^A = \begin{bmatrix} c_1 & 0 & 0 \\ c_2 & 1 & \frac{s}{1+s} \\ 0 & 0 & \frac{1}{1+s} \end{bmatrix} \tag{57}$$

and

$$\bar{\mathbf{C}}^B = \begin{bmatrix} \frac{s}{1+s} & 0 & 0 \\ \frac{1}{1+s} & 1 & c_3 \\ 0 & 0 & c_4 \end{bmatrix}, \tag{58}$$

where s is as defined in Eq. (50).

From that, we get

$$\left(\bar{\mathbf{C}}^A\right)^{-\mathsf{T}} \left(\mathbf{C}^A\right)^{\mathsf{T}} = \begin{bmatrix} 1 & 0 & 0 \\ 0 & 1 & 0 \\ 0 & -s & 1+s \end{bmatrix} \tag{59}$$

and

$$\left(\bar{\mathbf{C}}^B\right)^{-\mathsf{T}} \left(\mathbf{C}^B\right)^{\mathsf{T}} = \begin{bmatrix} \frac{1+s}{s} & -\frac{1}{s} & 0 \\ 0 & 1 & 0 \\ 0 & 0 & 1 \end{bmatrix}. \tag{60}$$

With that, we obtain

$$\bar{\tilde{\mathbf{x}}}_1^A = \tilde{\mathbf{x}}_1^A, \tag{61}$$

$$\bar{\tilde{\mathbf{x}}}_2^A = -s\tilde{\mathbf{x}}_1^A + (1+s)\tilde{\mathbf{x}}_2^A, \tag{62}$$

and

$$\bar{\mathbf{x}}_0^B = \frac{(1+s)\mathbf{x}_0^B - \mathbf{x}_1^B}{s}, \tag{63}$$

$$\bar{\mathbf{x}}_1^B = \mathbf{x}_1^B. \tag{64}$$

We substitute them into Eqs. (46) and (47), and obtain the following equations:

$$\tilde{\mathbf{x}}_1^A = \frac{(1+s)\mathbf{x}_0^B - \mathbf{x}_1^B}{s}, \tag{65}$$

$$-s\tilde{\mathbf{x}}_1^A + (1+s)\tilde{\mathbf{x}}_2^A = \mathbf{x}_1^B. \tag{66}$$

After some rearrangement, we get

$$\tilde{\mathbf{x}}_2^A = \mathbf{x}_0^B, \tag{67}$$

$$\tilde{\mathbf{x}}_2^A = \frac{s\tilde{\mathbf{x}}_1^A + \mathbf{x}_1^B}{s+1}. \tag{68}$$

References

1. Hughes TJR, Cottrell JA, Bazilevs Y (2005) Isogeometric analysis: CAD, finite elements, NURBS, exact geometry, and mesh refinement. Comput Methods Appl Mech Eng 194:4135–4195
2. Bazilevs Y, Calo VM, Zhang Y, Hughes TJR (2006) Isogeometric fluid–structure interaction analysis with applications to arterial blood flow. Comput Mech 38:310–322
3. Bazilevs Y, Calo VM, Hughes TJR, Zhang Y (2008) Isogeometric fluid–structure interaction: theory, algorithms, and computations. Comput Mech 43:3–37
4. Bazilevs Y, Hughes TJR (2008) NURBS-based isogeometric analysis for the computation of flows about rotating components. Comput Mech 43:143–150
5. Takizawa K, Tezduyar TE (2011) Multiscale space–time fluid-structure interaction techniques. Comput Mech 48:247–267. https://doi.org/10.1007/s00466-011-0571-z
6. Takizawa K, Henicke B, Puntel A, Spielman T, Tezduyar TE (2012) Space–time computational techniques for the aerodynamics of flapping wings. J Appl Mech 79:010903. https://doi.org/10.1115/1.4005073
7. Takizawa K, Tezduyar TE, Otoguro Y, Terahara T, Kuraishi T, Hattori H (2017) Turbocharger flow computations with the space–time isogeometric analysis (ST-IGA). Comput Fluids 142:15–20. https://doi.org/10.1016/j.compfluid.2016.02.021
8. Takizawa K, Tezduyar TE (2012) Space–time fluid–structure interaction methods. Math Models Methods Appl Sci 22(supp02):1230001. https://doi.org/10.1142/S0218202512300013
9. Takizawa K, Tezduyar TE, McIntyre S, Kostov N, Kolesar R, Habluetzel C (2014) Space–time VMS computation of wind-turbine rotor and tower aerodynamics. Comput Mech 53:1–15. https://doi.org/10.1007/s00466-013-0888-x
10. Takizawa K, Henicke B, Puntel A, Kostov N, Tezduyar TE (2012) Space–time techniques for computational aerodynamics modeling of flapping wings of an actual locust. Comput Mech 50:743–760. https://doi.org/10.1007/s00466-012-0759-x
11. Takizawa K, Kostov N, Puntel A, Henicke B, Tezduyar TE (2012) Space–time computational analysis of bio-inspired flapping-wing aerodynamics of a micro aerial vehicle. Comput Mech 50:761–778. https://doi.org/10.1007/s00466-012-0758-y
12. Bazilevs Y, Takizawa K, Tezduyar TE (2013) Computational fluid-structure interaction: methods and applications. Wiley, New York
13. Takizawa K, Tezduyar TE, Buscher A, Asada S (2014) Space–time interface-tracking with topology change (ST-TC). Comput Mech 54:955–971. https://doi.org/10.1007/s00466-013-0935-7
14. Takizawa K, Tezduyar TE, Buscher A (2015) Space–time computational analysis of MAV flapping-wing aerodynamics with wing clapping. Comput Mech 55:1131–1141. https://doi.org/10.1007/s00466-014-1095-0
15. Takizawa K, Bazilevs Y, Tezduyar TE (2022) Mesh moving methods in flow computations with the space–time and arbitrary Lagrangian–Eulerian methods. J Adv Eng Comput 6:85–112. https://doi.org/10.55579/jaec.202262.377
16. Takizawa K, Tezduyar TE (2014) Space–time computation techniques with continuous representation in time (ST-C). Comput Mech 53:91–99. https://doi.org/10.1007/s00466-013-0895-y
17. Takizawa K, Tezduyar TE, Kuraishi T (2015) Multiscale ST methods for thermo-fluid analysis of a ground vehicle and its tires. Math Models Methods Appl Sci 25:2227–2255. https://doi.org/10.1142/S0218202515400072
18. Takizawa K, Tezduyar TE (2016) New directions in space–time computational methods. In: Bazilevs Y, Takizawa K (eds) Advances in computational fluid–structure interaction and flow simulation: new methods and challenging computations, modeling and simu-

lation in science, engineering and technology. Springer, Berlin, pp 159–178. https://doi.org/10.1007/978-3-319-40827-9_13
19. Takizawa K, Tezduyar TE, Kuraishi T, Tabata S, Takagi H (2016) Computational thermo-fluid analysis of a disk brake. Comput Mech 57:965–977. https://doi.org/10.1007/s00466-016-1272-4
20. Komiya K, Kanai T, Otoguro Y, Kaneko M, Hirota K, Zhang Y, Takizawa K, Tezduyar TE, Nohmi M, Tsuneda T, Kawai M, Isono M (2019) Computational analysis of flow-driven string dynamics in a pump and residence time calculation. IOP Conf Ser Earth Environ Sci 240:062014. https://doi.org/10.1088/1755-1315/240/6/062014
21. Kanai T, Takizawa K, Tezduyar TE, Komiya K, Kaneko M, Hirota K, Nohmi M, Tsuneda T, Kawai M, Isono M (2019) Methods for computation of flow-driven string dynamics in a pump and residence time. Math Models Methods Appl Sci 29:839–870. https://doi.org/10.1142/S021820251941001X
22. Takizawa K, Bazilevs Y, Tezduyar TE, Korobenko A (2020) Variational multiscale flow analysis in aerospace, energy and transportation technologies. In: Grama A, Sameh A (eds) Parallel algorithms in computational science and engineering, modeling and simulation in science, engineering and technology. Springer, Berlin, pp 235–280. https://doi.org/10.1007/978-3-030-43736-7_8
23. Takizawa K, Bazilevs Y, Tezduyar TE, Korobenko A (2020) Computational flow analysis in aerospace, energy and transportation technologies with the variational multiscale methods. J Adv Eng Comput 4:83–117. https://doi.org/10.25073/jaec.202042.279
24. Bazilevs Y, Takizawa K, Tezduyar TE, Hsu M-C, Otoguro Y, Mochizuki H, Wu MCH (2020) Wind turbine and turbomachinery computational analysis with the ALE and space–time variational multiscale methods and isogeometric discretization. J Adv Eng Comput 4:1–32. https://doi.org/10.25073/jaec.202041.278
25. Bazilevs Y, Takizawa K, Tezduyar TE, Hsu M-C, Otoguro Y, Mochizuki H, Wu MCH (2020) ALE and space–time variational multiscale isogeometric analysis of wind turbines and turbomachinery. In: Grama A, Sameh A (eds) Parallel algorithms in computational science and engineering, modeling and simulation in science, engineering and technology. Springer, Berlin, pp 195–233. https://doi.org/10.1007/978-3-030-43736-7_7
26. Kuraishi T, Zhang F, Takizawa K, Tezduyar TE (2021) Wind turbine wake computation with the ST-VMS method, isogeometric discretization and multidomain method: I. Computational framework. Comput Mech 68:113–130. https://doi.org/10.1007/s00466-021-02022-4
27. Kuraishi T, Zhang F, Takizawa K, Tezduyar TE (2021) Wind turbine wake computation with the ST-VMS method, isogeometric discretization and multidomain method: II. Spatial and temporal resolution. Comput Mech 68:175–184. https://doi.org/10.1007/s00466-021-02025-1
28. Zhang F, Kuraishi T, Takizawa K, Tezduyar TE (2022) Wind turbine wake computation with the ST-VMS method and isogeometric discretization: directional preference in spatial refinement. Comput Mech 69:1031–1040. https://doi.org/10.1007/s00466-021-02129-8
29. Kuraishi T, Xu Z, Takizawa K, Tezduyar TE, Yamasaki S (2022) High-resolution multi-domain space–time isogeometric analysis of car and tire aerodynamics with road contact and tire deformation and rotation. Comput Mech. https://doi.org/10.1007/s00466-022-02228-0
30. Takizawa K, Tezduyar TE, Mochizuki H, Hattori H, Mei S, Pan L, Montel K (2015) Space–time VMS method for flow computations with slip interfaces (ST-SI). Math Models Methods Appl Sci 25:2377–2406. https://doi.org/10.1142/S0218202515400126
31. Korobenko A, Bazilevs Y, Takizawa K, Tezduyar TE (2018) Recent advances in ALE-VMS and ST-VMS computational aerodynamic and FSI analysis of wind turbines. In: Tezduyar TE (ed) Frontiers in computational fluid–structure interaction and flow simulation: research from lead investigators under forty—2018, modeling and simulation in science, engineering and technology. Springer, Berlin, pp 253–336. https://doi.org/10.1007/978-3-319-96469-0_7
32. Otoguro Y, Mochizuki H, Takizawa K, Tezduyar TE (2020) Space–time variational multiscale isogeometric analysis of a tsunami-shelter vertical-axis wind turbine. Comput Mech 66:1443–1460. https://doi.org/10.1007/s00466-020-01910-5
33. Bazilevs Y, Takizawa K, Tezduyar TE, Korobenko A, Kuraishi T, Otoguro Y (2022) Computational aerodynamics with isogeometric analysis. J Adv Eng Comput, to appear
34. Otoguro Y, Takizawa K, Tezduyar TE (2018) A general-purpose NURBS mesh generation method for complex geometries. In: Tezduyar TE (ed) Frontiers in computational fluid–structure interaction and flow simulation: research from lead investigators under forty—2018, modeling and simulation in science, engineering and technology. Springer, Berlin, pp 399–434. https://doi.org/10.1007/978-3-319-96469-0_10
35. Otoguro Y, Takizawa K, Tezduyar TE, Nagaoka K, Avsar R, Zhang Y (2019) Space–time VMS flow analysis of a turbocharger turbine with isogeometric discretization: computations with time-dependent and steady-inflow representations of the intake/exhaust cycle. Comput Mech 64:1403–1419. https://doi.org/10.1007/s00466-019-01722-2
36. Takizawa K, Montes D, Fritze M, McIntyre S, Boben J, Tezduyar TE (2013) Methods for FSI modeling of spacecraft parachute dynamics and cover separation. Math Models Methods Appl Sci 23:307–338. https://doi.org/10.1142/S0218202513400058
37. Liu Y, Takizawa K, Otoguro Y, Kuraishi T, Tezduyar TE (2022) Flow computation with the space–time isogeometric analysis and higher-order basis functions in time. Math Models Methods Appl Sci. https://doi.org/10.1142/S0218202522500579
38. Kuraishi T, Takizawa K, Tezduyar TE (2018) Space–time computational analysis of tire aerodynamics with actual geometry, road contact and tire deformation. In: Tezduyar TE (ed) Frontiers in computational fluid–structure interaction and flow simulation: research from lead investigators under forty—2018, modeling and simulation in science, engineering and technology. Springer, Berlin, pp 337–376. https://doi.org/10.1007/978-3-319-96469-0_8
39. Kuraishi T, Takizawa K, Tezduyar TE (2019) Tire aerodynamics with actual tire geometry, road contact and tire deformation. Comput Mech 63:1165–1185. https://doi.org/10.1007/s00466-018-1642-1
40. Kuraishi T, Takizawa K, Tezduyar TE (2019) Space–time computational analysis of tire aerodynamics with actual geometry, road contact, tire deformation, road roughness and fluid film. Comput Mech 64:1699–1718. https://doi.org/10.1007/s00466-019-01746-8
41. Tezduyar TE, Takizawa K, Kuraishi T (2022) Space-time computational FSI and flow analysis: 2004 and beyond. In: Aldakheel F, Hudobivnik B, Soleimani M, Wessels H, Weissenfels C, Marino M (eds) Current trends and open problems in computational mechanics. Springer, Berlin, pp 537–544. https://doi.org/10.1007/978-3-030-87312-7_52
42. Kuraishi T, Yamasaki S, Takizawa K, Tezduyar TE, Xu Z, Kaneko R (2022) Space–time isogeometric analysis of car and tire aerodynamics with road contact and tire deformation and rotation. Comput Mech 70:49–72. https://doi.org/10.1007/s00466-022-02155-0
43. Kuraishi T, Terahara T, Takizawa K, Tezduyar TE (2022) Computational flow analysis with boundary layer and contact representation: I. Tire aerodynamics with road contact. J Mech 38:77–87. https://doi.org/10.1093/jom/ufac009
44. Kuraishi T, Takizawa K, Tezduyar TE (2019) Space–time isogeometric flow analysis with built-in Reynolds-equation limit. Math

Models Methods Appl Sci 29:871–904. https://doi.org/10.1142/S0218202519410021
45. Takizawa K, Tezduyar TE, Terahara T (2016) Ram-air parachute structural and fluid mechanics computations with the space–time isogeometric analysis (ST-IGA). Comput Fluids 141:191–200. https://doi.org/10.1016/j.compfluid.2016.05.027
46. Kanai T, Takizawa K, Tezduyar TE, Tanaka T, Hartmann A (2019) Compressible-flow geometric-porosity modeling and spacecraft parachute computation with isogeometric discretization. Comput Mech 63:301–321. https://doi.org/10.1007/s00466-018-1595-4
47. Takizawa K, Tezduyar TE, Terahara T, Sasaki T (2018) Heart valve flow computation with the space–time slip interface topology change (ST-SI-TC) method and isogeometric analysis (IGA). In: Wriggers P, Lenarz T (eds) Biomedical technology: modeling, experiments and simulation. Lecture notes in applied and computational mechanics. Springer, Berlin, pp 77–99. https://doi.org/10.1007/978-3-319-59548-1_6
48. Takizawa K, Tezduyar TE, Terahara T, Sasaki T (2017) Heart valve flow computation with the integrated space–time VMS, slip interface, topology change and isogeometric discretization methods. Comput Fluids 158:176–188. https://doi.org/10.1016/j.compfluid.2016.11.012
49. Takizawa K, Tezduyar TE, Uchikawa H, Terahara T, Sasaki T, Shiozaki K, Yoshida A, Komiya K, Inoue G (2018) Aorta flow analysis and heart valve flow and structure analysis. In: Tezduyar TE (ed) Frontiers in computational fluid–structure interaction and flow simulation: research from lead investigators under forty—2018, modeling and simulation in science, engineering and technology. Springer, Berlin, pp 29–89. https://doi.org/10.1007/978-3-319-96469-0_2
50. Takizawa K, Tezduyar TE, Uchikawa H, Terahara T, Sasaki T, Yoshida A (2019) Mesh refinement influence and cardiac-cycle flow periodicity in aorta flow analysis with isogeometric discretization. Comput Fluids 179:790–798. https://doi.org/10.1016/j.compfluid.2018.05.025
51. Takizawa K, Bazilevs Y, Tezduyar TE, Hsu M-C (2019) Computational cardiovascular flow analysis with the variational multiscale methods. J Adv Eng Comput 3:366–405. https://doi.org/10.25073/jaec.201932.245
52. Hughes TJR, Takizawa K, Bazilevs Y, Tezduyar TE, Hsu M-C (2020) Computational cardiovascular analysis with the variational multiscale methods and isogeometric discretization. In: Grama A, Sameh A (eds) Parallel algorithms in computational science and engineering, modeling and simulation in science, engineering and technology. Springer, Berlin, pp 151–193. https://doi.org/10.1007/978-3-030-43736-7_6
53. Terahara T, Takizawa K, Tezduyar TE, Bazilevs Y, Hsu M-C (2020) Heart valve isogeometric sequentially-coupled FSI analysis with the space–time topology change method. Comput Mech 65:1167–1187. https://doi.org/10.1007/s00466-019-01813-0
54. Terahara T, Takizawa K, Tezduyar TE, Tsushima A, Shiozaki K (2020) Ventricle-valve-aorta flow analysis with the space–time isogeometric discretization and topology change. Comput Mech 65:1343–1363. https://doi.org/10.1007/s00466-020-01822-4
55. Takizawa K, Terahara T, Tezduyar TE (2022) Space–time flow computation with contact between the moving solid surfaces. In: Aldakheel F, Hudobivnik B, Soleimani M, Wessels H, Weissenfels C, Marino M (eds) Current trends and open problems in computational mechanics. Springer, Berlin, pp 517–525. https://doi.org/10.1007/978-3-030-87312-7_50
56. Terahara T, Kuraishi T, Takizawa K, Tezduyar TE (2022) Computational flow analysis with boundary layer and contact representation: II. Heart valve flow with leaflet contact. J Mech 38:185–194. https://doi.org/10.1093/jom/ufac013
57. Takizawa K, Bazilevs Y, Tezduyar TE, Hsu M-C, Terahara T (2022) Computational cardiovascular medicine with isogeometric analysis. J Adv Eng Comput 6:167–199. https://doi.org/10.55579/jaec.202263.381
58. Aydinbakar L, Takizawa K, Tezduyar TE, Kuraishi T (2021) Space–time VMS isogeometric analysis of the Taylor–Couette flow. Comput Mech 67:1515–1541. https://doi.org/10.1007/s00466-021-02004-6
59. Kuraishi T, Takizawa K, Tezduyar TE (2022) Boundary layer mesh resolution in flow computation with the space–time variational multiscale method and isogeometric discretization. Math Models Methods Appl Sci. https://doi.org/10.1142/S0218202522500567
60. Liu Y, Takizawa K, Tezduyar TE, Kuraishi T, Zhang Y (2022) Carrier-domain method for high-resolution computation of time-periodic long-wake flows. Comput Mech. https://doi.org/10.1007/s00466-022-02230-6
61. Tezduyar TE, Cragin T, Sathe S, Nanna B (2007) FSI computations in arterial fluid mechanics with estimated zero-pressure arterial geometry. In: Onate E, Garcia J, Bergan P, Kvamsdal T (eds) Marine 2007. CIMNE, Barcelona, Spain
62. Takizawa K, Tezduyar TE, Sasaki T (2018) Estimation of element-based zero-stress state in arterial FSI computations with isogeometric wall discretization. In: Wriggers P, Lenarz T (eds) Biomedical technology: modeling, experiments and simulation. Lecture notes in applied and computational mechanics. Springer, Berlin, pp 101–122. https://doi.org/10.1007/978-3-319-59548-1_7
63. Takizawa K, Tezduyar TE, Sasaki T (2017) Aorta modeling with the element-based zero-stress state and isogeometric discretization. Comput Mech 59:265–280. https://doi.org/10.1007/s00466-016-1344-5
64. Sasaki T, Takizawa K, Tezduyar TE (2019) Aorta zero-stress state modeling with T-spline discretization. Comput Mech 63:1315–1331. https://doi.org/10.1007/s00466-018-1651-0
65. Sasaki T, Takizawa K, Tezduyar TE (2019) Medical-image-based aorta modeling with zero-stress-state estimation. Comput Mech 64:249–271. https://doi.org/10.1007/s00466-019-01669-4
66. Takizawa K, Tezduyar TE, Sasaki T (2019) Isogeometric hyperelastic shell analysis with out-of-plane deformation mapping. Comput Mech 63:681–700. https://doi.org/10.1007/s00466-018-1616-3
67. Taniguchi Y, Takizawa K, Otoguro Y, Tezduyar TE (2022) A hyperelastic extended Kirchhoff–Love shell model with out-of-plane normal stress: I. Out-of-plane deformation. Comput Mech 70:247–280. https://doi.org/10.1007/s00466-022-02166-x
68. Bazilevs Y, Hsu M-C, Kiendl J, Benson DJ (2012) A computational procedure for pre-bending of wind turbine blades. Int J Numer Methods Eng 89:323–336
69. Bazilevs Y, Deng X, Korobenko A, di Scalea FL, Todd MD, Taylor SG (2015) Isogeometric fatigue damage prediction in large-scale composite structures driven by dynamic sensor data. J Appl Mech 82:091008
70. Kiendl J, Hsu M-C, Wu MCH, Reali A (2015) Isogeometric Kirchhoff–Love shell formulations for general hyperelastic materials. Comput Methods Appl Mech Eng 291:280–303
71. Hsu M-C, Wang C, Herrema AJ, Schillinger D, Ghoshal A, Bazilevs Y (2015) An interactive geometry modeling and parametric design platform for isogeometric analysis. Comput Math Appl 70:1481–1500
72. Herrema AJ, Wiese NM, Darling CN, Ganapathysubramanian B, Krishnamurthy A, Hsu M-C (2017) A framework for parametric design optimization using isogeometric analysis. Comput Methods Appl Mech Eng 316:944–965
73. Benzaken J, Herrema AJ, Hsu M-C, Evans JA (2017) A rapid and efficient isogeometric design space exploration framework with application to structural mechanics. Comput Methods Appl Mech Eng 316:1215–1256
74. Kamensky D, Xu F, Lee C-H, Yan J, Bazilevs Y, Hsu M-C (2018) A contact formulation based on a volumetric potential: application to

isogeometric simulations of atrioventricular valves. Comput Methods Appl Mech Eng 330:522–546
75. Herrema AJ, Johnson EL, Proserpio D, Wu MCH, Kiendl J, Hsu M-C (2019) Penalty coupling of non-matching isogeometric Kirchhoff–Love shell patches with application to composite wind turbine blades. Comput Methods Appl Mech Eng 346:810–840
76. Herrema AJ, Kiendl J, Hsu M-C (2019) A framework for isogeometric-analysis-based optimization of wind turbine blade structures. Wind Energy 22:153–170
77. Johnson EL, Hsu M-C (2020) Isogeometric analysis of ice accretion on wind turbine blades. Comput Mech 66:311–322
78. Kiendl J, Bazilevs Y, Hsu M-C, Wüchner R, Bletzinger K-U (2010) The bending strip method for isogeometric analysis of Kirchhoff-Love shell structures comprised of multiple patches. Comput Methods Appl Mech Eng 199:2403–2416
79. Raknes SB, Deng X, Bazilevs Y, Benson DJ, Mathisen KM, Kvamsdal T (2013) Isogeometric rotation-free bending-stabilized cables: statics, dynamics, bending strips and coupling with shells. Comput Methods Appl Mech Eng 263:127–143
80. Johnson EL, Laurence DW, Xu F, Crisp CE, Mir A, Burkhart HM, Lee C-H, Hsu M-C (2021) Parameterization, geometric modeling, and isogeometric analysis of tricuspid valves. Comput Methods Appl Mech Eng 384:113960
81. Nitsche J (1971) Über ein variationsprinzip zur lösung von Dirichlet-problemen bei verwendung von teilräumen, die keinen randbedingungen unterworfen sind. Abhandlungen aus dem Mathematischen Seminar der Universität Hamburg 36:9–15
82. Sederberg T, Zheng J, Bakenov A, Nasri A (2003) T-splines and T-NURCCs. ACM Trans Graph (TOG) 22:477–484
83. Otoguro Y, Takizawa K, Tezduyar TE (2020) Element length calculation in B-spline meshes for complex geometries. Comput Mech 65:1085–1103. https://doi.org/10.1007/s00466-019-01809-w
84. Ueda Y, Otoguro Y, Takizawa K, Tezduyar TE (2020) Element-splitting-invariant local-length-scale calculation in B-spline meshes for complex geometries. Math Models Methods Appl Sci 30:2139–2174. https://doi.org/10.1142/S0218202520500402
85. Roddeman DG, Drukker J, Oomens CWJ, Janssen JD (1987) The wrinkling of thin membranes: part I-theory. J Appl Mech 54:884–887